

Fractal basins of escape and the formation of spiral arms in a galactic potential with a bar

Andreas Ernst^{1*} and Thomas Peters^{2†}

¹*Astronomisches Rechen-Institut/Zentrum für Astronomie der Universität Heidelberg, Mönchhofstrasse 12-14, 69120 Heidelberg, Germany*

²*Institut für Computergestützte Wissenschaften, Universität Zürich, Winterthurerstrasse 190, CH-8057 Zürich, Switzerland*

Accepted ... Received ...

ABSTRACT

We investigate the dynamics in the close vicinity of and within the critical area in a 2D effective galactic potential with a bar of Zotos. We have calculated Poincaré surfaces of section and the basins of escape. In both the Poincaré surfaces of section and the basins of escape we find numerical evidence for the existence of a separatrix which hinders orbits from escaping out of the bar region. We present numerical evidence for the similarity between spiral arms of barred spiral galaxies and tidal tails of star clusters.

Key words: Galaxies – Stellar dynamics

1 INTRODUCTION

Many spiral galaxies have barred central regions. It has been established by de Vaucouleurs (1963) that roughly one third of disk galaxies are strongly barred, one third do not have a bar, and the remaining third are, with respect to having the bar property, of intermediate or undeterminable type.

There was a long controversy whether the bar fraction of barred to disk galaxies is red-shift-dependent. Recent results suggest indeed that the fraction of barred spirals declines with redshift (Sheth et al. 2008; Masters et al. 2011; Melvin et al. 2013).

The stellar-dynamical reason for the occurrence of bars is believed to be a dynamical instability in rotationally supported stellar discs (Miller et al. 1970; Hohl 1971; Ostriker & Peebles 1973; Sellwood 1980). In particular, if the ratio of rotational to random kinetic energies exceeds a certain threshold, an initially axisymmetric stellar system is unstable to the formation of a bar-like mode, i.e. a non-axisymmetric perturbation.

The present study aims at numerically investigating the dynamics in the vicinity of a bar in the centre of a galaxy. In the language of dynamical systems theory, the issue amounts to examining bound and unbound orbits in a two-dimensional Hamiltonian system. The problem of escape from Hamiltonian systems is a classical problem in dynamical astronomy and nonlinear dynamics (e.g. Contopoulos 1990; Contopoulos & Kaufmann 1992; Contopoulos et al. 1993, 2012; Siopis et al. 1996; Navarro & Henrard 2001; Schneider et al. 2002; Ernst et al. 2008). However, it is far

less studied than the closely related situation of chaotic scattering, where a body from infinity approaches and scatters off a complex potential. This problem is well understood from the viewpoint of chaos theory (e.g. Bleher et al. 1989, 1990; Boyd & McMillan 1992, 1993; Chen et al. 1990; Ding et al. 1990; Eckhardt & Jung 1986; Eckhardt 1987, 1988; Gaspard & Rice 1989; Hénon 1988; José et al. 1992; Jung 1987; Jung & Scholz 1987; Jung & Pott 1989; Jung & Richter 1990; Jung & Tel 1991; Jung et al. 1995, 1999; Lai et al. 1993, 2000; Lau et al. 1991; Lipp & Jung 1999; Motter & Lai 2002; Rückerl & Jung 1994; Seoane et al. 2006, 2007; Seoane & Sanjuán 2008; Sweet & Ott 2000) and has been applied in the astrophysical context to, e.g., the scattering off black holes (e.g. Aguirregabiria 1997; de Moura & Letelier 2000) and three-body systems (e.g. Hut & Bahcall 1983; Hut 1983; Benet et al. 1999, 1996).

We here do not study in detail individual orbits of stars within the galactic potential and Poincaré sections (e.g. Athanassoula et al. 1983; Caranicolas & Karanis 1998; Contopoulos & Papayannopoulos 1980; Contopoulos 1983b,a; Contopoulos et al. 1987; Hasan & Norman 1990; Hasan et al. 1993; Hénon & Heiles 1964; Martinet & Udry 1990; Pfenniger 1984; Teuben & Sanders 1985; Zotos 2011, 2012b,c,a), but rather focus on the computation of the basins of escape, the related invariant manifolds of the chaotic saddle associated with the chaotic dynamical behaviour (e.g. Ott 2002) and the formation of spiral structure as a result of the escape process.

The basins of escape are defined as those initial conditions (e.g., on a surface of section) for which particles escape through exits in the equipotential surfaces around the Lagrangian points L_1 and L_2 . These exits open up for Jacobi energies which are higher than the critical Jacobi energy.

* email: aernst@ari.uni-heidelberg.de

† email: tpeters@physik.uzh.ch

The critical Jacobi energy is defined to be the effective potential at the Lagrangian points L_1 and L_2 . The boundaries between the basins of escape may be fractal (Bleher et al. 1988) or, as is the case for the widely known Hénon-Heiles system (Hénon & Heiles 1964), respect the more restrictive property of Wada (Aguirre et al. 2001) in the case of three or more coexisting basins of escape.

The stable (or unstable) manifolds of the chaotic saddle are defined as the set of points on the boundaries between the basins of escape, for which orbits do not escape for $t \rightarrow \infty$ (or $t \rightarrow -\infty$). The chaotic saddle is defined as the intersection of its stable and unstable manifolds. The intersection points between the stable and unstable manifolds of the chaotic saddle are also called biasymptotic points (c.f. Simó 2014). Both hyperbolic and non-hyperbolic chaotic saddles occur in dynamical systems (e.g. Lai et al. 1993). A non-hyperbolic chaotic saddle may display vanishing splitting angles between the stable and unstable manifolds (Lai et al. 1993). This phenomenon is called a tangency.

In this context, it is worth mentioning that invariant manifolds of the Lyapunov orbits (Lyapunov 1949) around the Lagrangian points L_1 and L_2 have been invoked recently to explain the formation of rings and spirals in barred galaxies (Romero-Gómez et al. 2006, 2007; Athanassoula et al. 2009a,b, 2010, 2011; Athanassoula 2012). These consist of orbits which approach the unstable periodic Lyapunov orbits around L_1/L_2 asymptotically for $t \rightarrow +\infty$ or $t \rightarrow -\infty$. A few of these asymptotic orbits are shown in Figure 8 of Fukushima & Heggie (2000).

We refer to Seoane & Sanjuán (2013), Aguirre et al. (2009) and Altmann et al. (2013) for recent reviews on chaotic scattering, fractal basins and escape from chaotic systems, respectively.

This paper is organised as follows. In Section 2 we present the theory. In section 3 we discuss the results: Poincaré surfaces of section (section 3.1), orbits (section 3.2), basins of escape (section 3.3) and spiral arms (section 3.4). We summarise our conclusions in Section 4.

2 THEORY

We adopt the effective potential of Zotos (2012b), which is visualised in Figure 1,

$$\begin{aligned} \Phi_{\text{eff}}(x, y) = & -\frac{M_d}{\sqrt{x^2 + y^2 + \alpha^2}} - \frac{M_b}{\sqrt{x^2 + b^2y^2 + c_b^2}} \\ & - \frac{M_n}{\sqrt{x^2 + y^2 + c_n^2}} + \frac{v_0^2}{2} \ln(x^2 + \beta y^2 + c_h^2) \\ & - \frac{1}{2} \Omega_b^2 (x^2 + y^2) \end{aligned} \quad (1)$$

with the parameters $\alpha = 8$, $\beta = 1.3$, $b = 2$, $v_0 = 15$, $M_d = 9500$, $M_b = 3000$, $M_n = 400$, $c_b = 1.5$, $c_n = 0.25$ and $c_h = 8.5$. We have $\Omega_b = 1.25$. The model consists of a disc, a bar, a Plummer nucleus (bulge) and a logarithmic halo. The bar rotates clockwise at constant angular velocity Ω_b . The effective potential in Eqn. (1) is the cut through the equatorial plane of a typical 3D potential of a barred spiral galaxy. The parameters for all calculations in the present paper are chosen as in Zotos (2012b). While the parameter b determines the elongation of the bar, β determines the

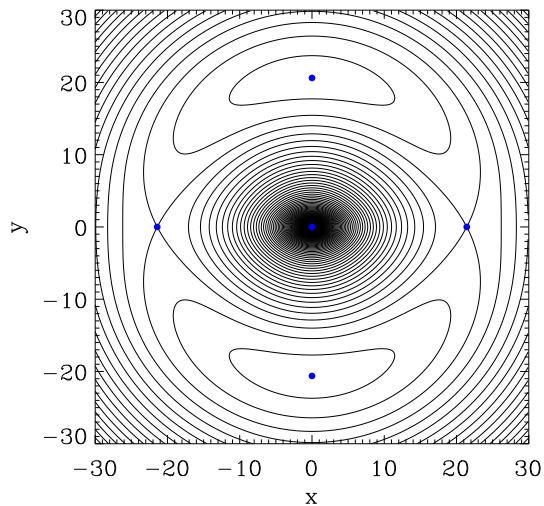


Figure 1. The effective potential of Eqn. (1) in 2D. The contours are the isolines of constant effective potential. The Lagrangian equilibrium points are visualized with (blue) dots.

elongation of the halo. The weak effect of removing the non-axisymmetry in the halo by setting $\beta = 1.0$ is shown as follows: The positions of the Lagrangian points L_4 and L_5 within the banana-shaped isolines of the effective potential in Figure 1 are $(x, y) = (0, \pm 20.619528162205612)$ for $\beta = 1.3$ and $(x, y) = (0, \pm 20.532965314242505)$ for $\beta = 1.0$. The relative difference is $\Delta y/y = 4.2 \times 10^{-3}$, which is tiny.

In Eqn. (1), the model units of length L_0 , velocity V_0 , angular velocity Ω_0 , time T_0 and mass M_0 of the parameters, in which the gravitational constant $G = 1$, can be scaled to physical units of a barred spiral galaxy with the size of a galaxy such as NGC 1300 as follows:

$$L_0 = 1 \text{ kpc}, \quad M_0 \approx 2.223 \times 10^7 M_\odot, \quad (2)$$

$$\Omega_0 = 10 \text{ km/s/kpc}, \quad V_0 = 10 \text{ km/s}, \quad (3)$$

$$T_0 = \sqrt{L_0^3 / (GM_0)} \approx 100 \text{ Myr}. \quad (4)$$

In these physical units, the circular speed in the halo is $v_0 = 150$ km/s, the mass of the disk is $M_d \approx 2 \times 10^{11} M_\odot$ and the length of the bar is $2r_L \approx 42$ kpc.

The equations of motion in the rotating frame are given by

$$\ddot{\mathbf{r}} = -\nabla \Phi_{\text{eff}} - 2(\Omega_b \times \dot{\mathbf{r}}) \quad (5)$$

$$= -\nabla \Phi - 2(\Omega_b \times \dot{\mathbf{r}}) - \Omega_b \times (\Omega_b \times \mathbf{r}) \quad (6)$$

where $\mathbf{r} = (x, y, z)$ is the position vector, the dot denotes a derivative with respect to time and Φ is given by the first four terms in (1) (i.e., without the last centrifugal potential term). Since we are considering a 2D case we set $z = 0$ or neglect it.

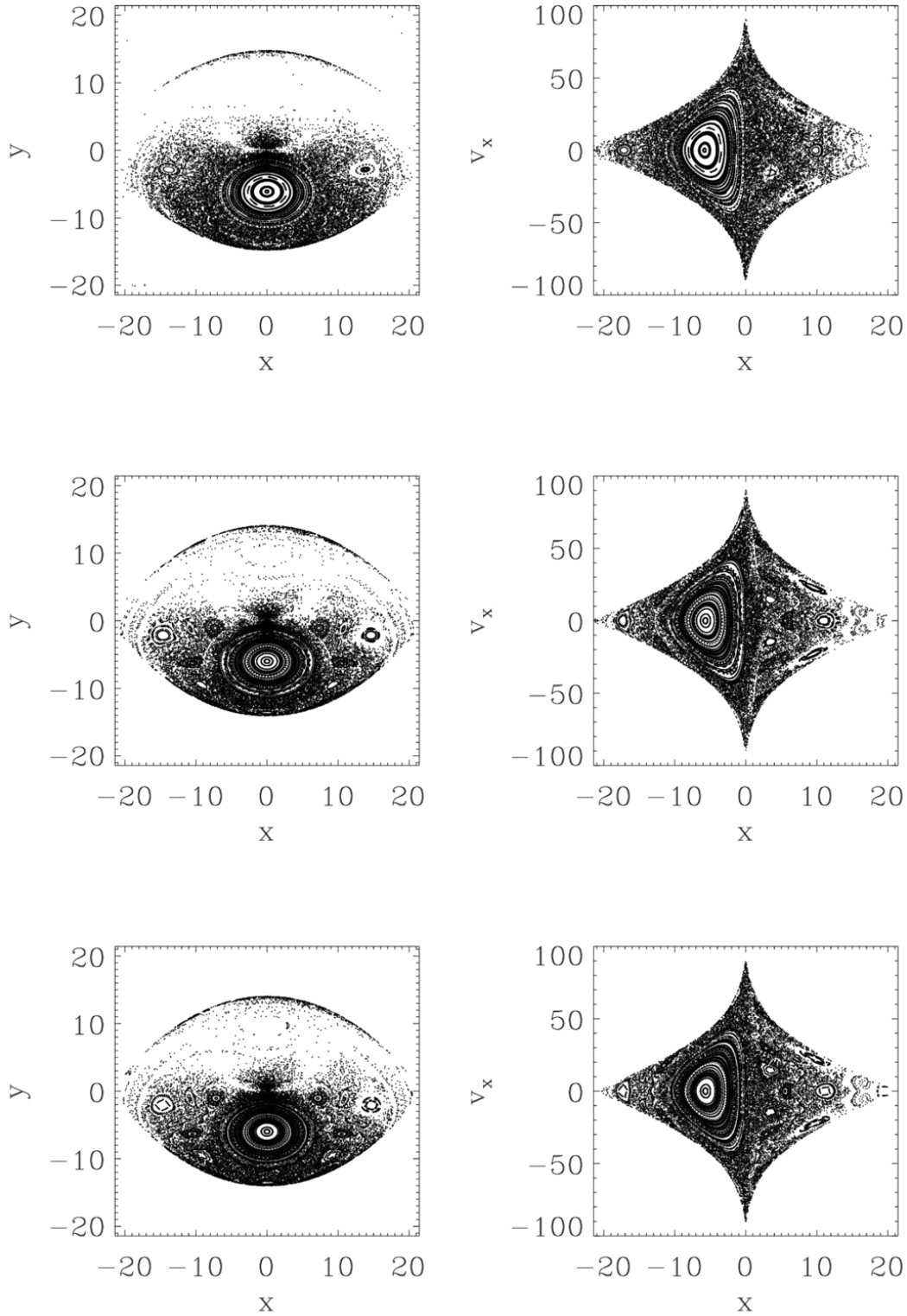


Figure 3. Poincaré surfaces of section at $e_J = -203.75205349030903$ (top panel), -224.12725883933993 (middle panel), -226.16477937424302 (bottom panel). Left panels: Crossing $\dot{y} = 0$ with $\dot{x} \geq 0$. Right panels: Crossing $y = 0$ with $\dot{y} \leq 0$.

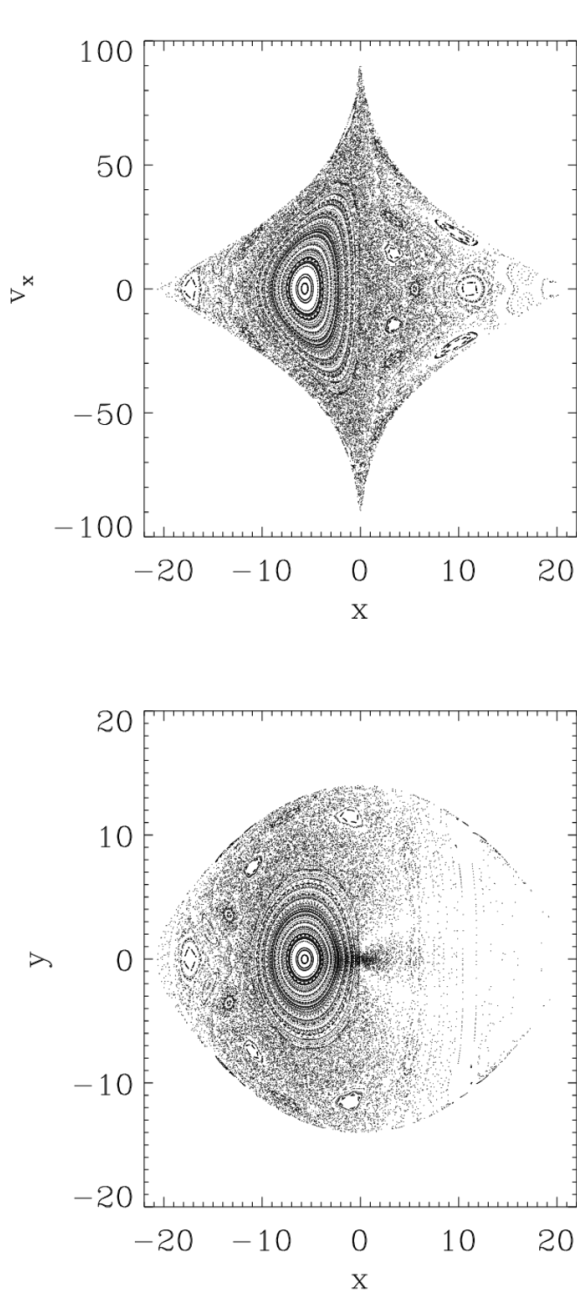


Figure 2. Poincaré surfaces of section at $e_{J,\text{crit}} = -226.391170544787810$. Top panel: Crossing $y = 0$ with $\dot{y} \leq 0$. Bottom panel: Crossing $\dot{x} = 0$ with $\dot{y} \leq 0$.

The Lagrangian points L_1 and L_2 are defined by the condition

$$\ddot{\mathbf{r}} = -\nabla_{2D}\Phi_{\text{eff}} = \begin{pmatrix} 0 \\ 0 \end{pmatrix} \quad (7)$$

where $\mathbf{r} = (x, y)$, $\nabla_{2D} = (\partial/\partial x, \partial/\partial y)$ and by the fact that they are saddle points of the effective potential, i.e. the two eigenvalues of the corresponding 2×2 Jacobi matrix at L_1 and L_2 are real and differ in sign. In the case of the effective potential of Eqn. (1) L_1 and L_2 are located at

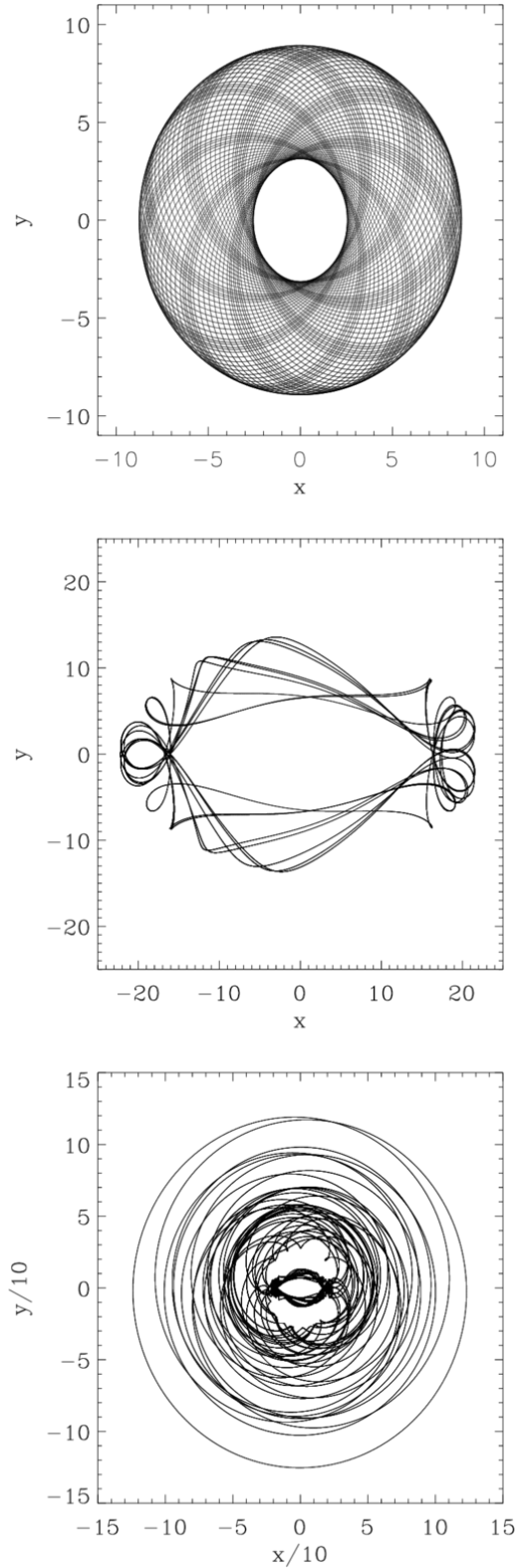


Figure 4. Four orbits. Top panel: Non-escaping retrograde quasiperiodic rosette orbit at $e_{J,\text{crit}}$ with $(x_0, y_0, v_{x0}) = (-3, 4, 0)$. Middle panel: Non-escaping chaotic orbit at $e_J = -203.75205349030903$ with $(x_0, y_0, v_{x0}) = (-16, 0, 0)$. Bottom panel: Escaping chaotic orbit at $e_J = -210$ with $(x_0, y_0, v_{x0}) = (20.8, 0, 5)$.

$(x, y) = (0, \pm r_L) = (0, \pm 21.417693579040430)$. r_L is called Lagrangian radius. Let L_1 be at $x = -r_L$ and L_2 be at $x = +r_L$. In Figure 1, there is a local minimum of the effective potential at $(x, y) = (0, 0)$, which is usually called L_3 , and two local maxima (L_4 and L_5) enclosed by the banana-shaped isolines of the effective potential.

In the 3D case, the last closed equipotential surface through L_1 and L_2 encloses the critical volume (in the 2D case it reduces to a critical area). In the context of star cluster, binary star or planetary dynamics, respectively, it is sometimes called Jacobi, Roche or Hill volume, respectively. The Jacobi energy is an isolating integral of motion and defined by

$$e_J = \frac{\dot{\mathbf{r}}^2}{2} + \Phi_{\text{eff}} \quad (8)$$

The critical Jacobi energy is given by $e_{J,\text{crit}} = \Phi_{\text{eff}}(r_L) = -226.39117054478781$. It is the effective potential of Eqn. (1) evaluated at the Lagrange points L_1 and L_2 . Orbits with $e_J < e_{J,\text{crit}}$ are bound and cannot escape since there are no exits in the equipotential surfaces around L_1 and L_2 . If one increases the Jacobi energy for $e_J > e_{J,\text{crit}}$ the exits around L_1 and L_2 in the equipotential surfaces become larger. We examine only situations with $e_J \geq e_{J,\text{crit}}$, since we study the escape process from the bar region.

We use in the present paper an eighth-order Runge-Kutta method for the orbit integrations.

3 RESULTS

3.1 Poincaré surfaces of section

The Poincaré surfaces of section are 2D cuts through the 4D phase space. For example, for an $x - v_x$ surface of section as in the top panel of Figure 2 we take an initial condition $x = x_0, v_x = v_{x,0}, y = y_0 = 0$ and choose v_y positively as $v_y = \sqrt{2e_J - v_x^2 - 2\Phi_{\text{eff}}(x_0, y_0)}$. Then we integrate the initial condition forwards in time and plot a dot at each consequent (=“piercing point through the surface of section”) with $y = 0$ when $v_y \leq 0$.

Figure 2 shows two Poincaré surfaces of section at the critical Jacobi energy. The top panel shows orbits crossing $y = 0$ with $\dot{y} \leq 0$. The bottom panel shows orbits crossing $\dot{x} = 0$ with $\dot{y} \leq 0$.

Figure 3 shows Poincaré surfaces of section at $e_J = -203.75205349030903$ (top panel), -224.12725883933993 (middle panel), -226.16477937424302 (bottom panel). These values of the Jacobi energy correspond to the relative deviations from the critical Jacobi energy ($(e_J - e_{J,\text{crit}})/e_{J,\text{crit}} = 0.1, 0.01$ and 0.001 as in Ernst et al. (2008).

The following aspects are similarly found in the paradigmatic Hénon-Heiles system (Hénon & Heiles 1964):

(i) In some regions an adelic integral of motion is present which hinders the particles on quasiperiodic orbits from escaping.

(ii) In Figure 3, it can be seen that with growing e_J , regular islands in the Poincaré surfaces of section disappear and are replaced with regions that show a chaotic dynamical behaviour.

(iii) Some areas on the surfaces of section in the “chaotic

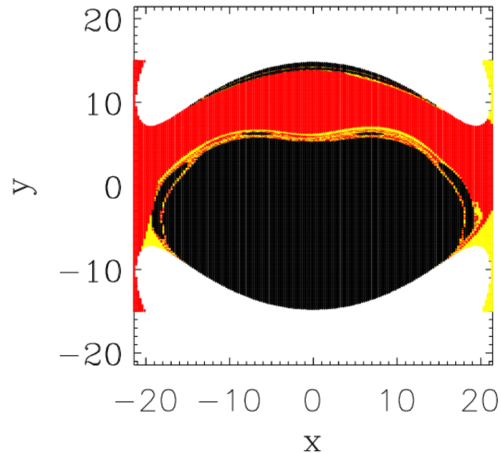


Figure 6. Backwards integration at $e_J = -203.75205349030903$. The red (and yellow) regions correspond to initial conditions for which the escaping star passes L_1 (or L_2). The black regions correspond to initial conditions for which the orbit does not escape.

sea” are less densely occupied by chaotic stellar orbits than others.

Regarding aspect (iii), it must be noted that, for $e_J > e_{J,\text{crit}}$, the reason may be the fact that particles can leak out through exits in the equipotential surfaces (as in the upper right panel of Figure 2 of Ernst et al. 2008).

However, Figures 5 and 7 below confirm that a large subset of particles, which includes even the chaotic orbits, cannot leak out at all and is trapped within a separatrix. In this case the fact that some regions are less densely populated by stellar orbits must have a different explanation. We found such a phenomenon also in our previous work (Ernst et al. 2008).

We have also verified that the Poincaré surfaces of section at $e_J = -570$ and $e_J = -2700$ are consistent with Figures 2 and 4 in Zotos (2012b).

3.2 Orbits

In total, Figure 4 shows three orbits. The top panel shows a non-escaping retrograde quasiperiodic rosette orbit at $(x_0, y_0, v_{x0}) \approx (-3, 4, 0)$ at $e_{J,\text{crit}}$. The middle panel shows a non-escaping chaotic orbit at $e_J = -203.75205349030903$ with $(x_0, y_0, v_{x0}) = (-16, 0, 0)$. The bottom panel shows a typical example of an escaping chaotic orbit at $e_J = -210$ with $(x_0, y_0, v_{x0}) = (20.8, 0, 5)$.

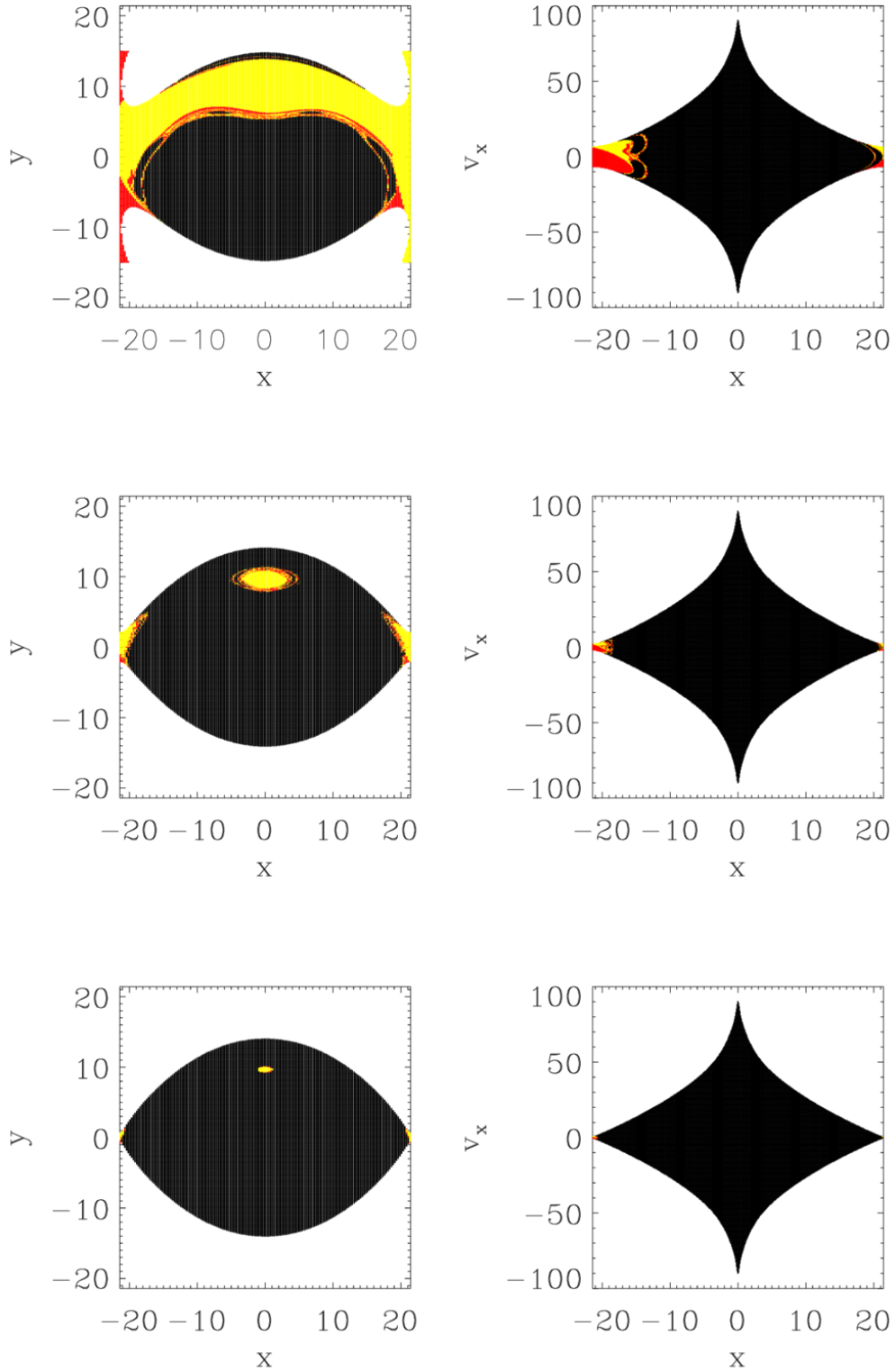


Figure 5. Basins of escape at $e_J = -203.75205349030903$ (top panel), -224.12725883933993 (middle panel), -226.16477937424302 (bottom panel). The red (and yellow) regions correspond to initial conditions for which the escaping star passes L_1 (or L_2). The black regions correspond to initial conditions for which the orbit does not escape.

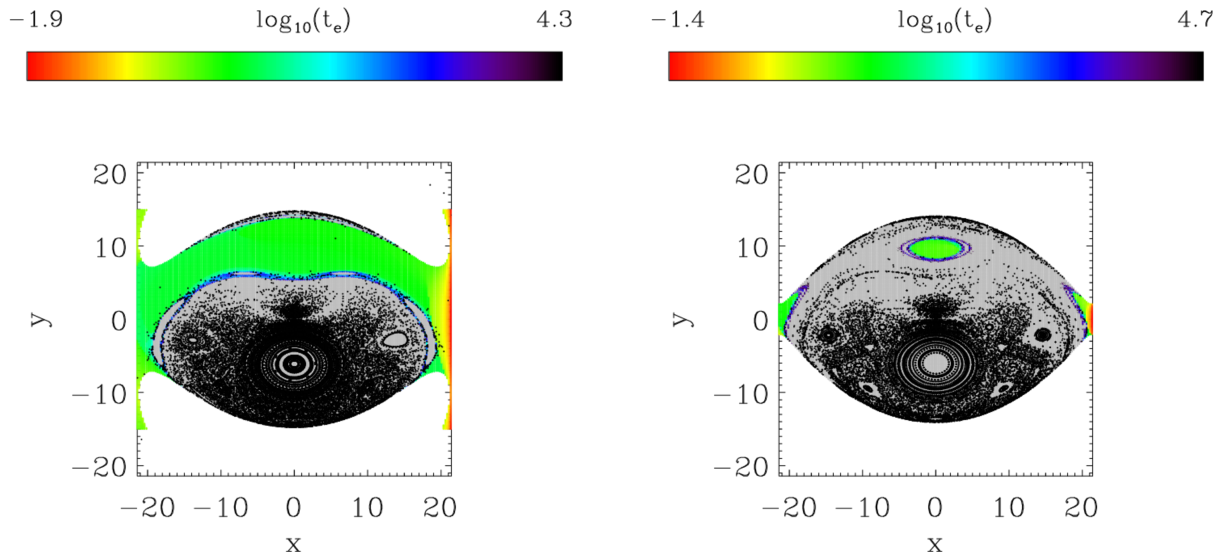


Figure 7. Distributions of escape times on surfaces of section. Left panel: At $e_J = -203.75205349030903$. Right panel: At $e_J = -224.12725883933993$. The scale on the color bar is logarithmic. The region within the separatrix, from which orbits do not escape, is overlaid with black dots and invariant curves on the grey-shaded area.

3.3 Basins of escape

Figure 5 shows the basins of escape for the same parameters as in Figure 3, i.e. for $e_J > e_{J,\text{crit}}$.

For each panel on the left-hand side of Figure 5 between 60000 and 80000 orbits have been integrated on a rectangular grid of size $N_x \times N_y \approx 2r_L/\Delta x \times (4/3)r_L/\Delta y$ of initial conditions on the Poincaré surface of section with cell side lengths $\Delta x = 0.25$ and $\Delta y = 0.05$. The grid is centered in the origin of phase space coordinates. For comparison, for each panel on the right-hand side of Figure 5 between 49000 and 52000 orbits have been integrated on a similar rectangular grid. For simplicity, our initial conditions for the calculation of the basins of escape cover both quasiperiodic and chaotic areas of the corresponding surface of section. We remark that, in principle, it is not necessary to integrate the orbits in areas with quasiperiodic orbits, since we know that these do not escape. Also, we do not consider all initial conditions in the same chaotic sea as one and the same orbit. We calculated the initial conditions for the velocities in the same way as for the Poincaré surfaces of section in Section 3.1.

In Figure 5, the red (and yellow) regions correspond to initial conditions for which the escaping star passes the Lagrangian point L_1 (or L_2) while it escapes. This passing-by condition defines the basins of escape. We call the corresponding basins of escape, which can be visualised on the surfaces of section, the L_1 - (or L_2 -) basins of escape. The black regions correspond to initial conditions where the orbits are trapped and do not escape. The time of escape t_e for the red and yellow regions is defined as the time when the escaping star passes the vertical line given by $(x, y) = (\pm r_L, y)$. As the black regions of Figure 5 are concerned, we consider an initial condition as non-escaping if its orbit remains bound for longer than $t_{\text{max}} = 20000$ (top

panels), $t_{\text{max}} = 50000$ (middle panels) or $t_{\text{max}} = 100000$ (bottom panels). The missing symmetry of the basins of escape with respect to the x and y axes are due to the choice of a subset of orbits with a fixed sign of one component of the velocity vector. An inspection of Figure 5 reveals that for energies close to the critical Jacobi energy (and, of course, for energies below the critical Jacobi energy) the allowed phase space volume is coloured black to a large extent (or nearly totally).

To estimate the size of the chaotic saddle, Figure 6 shows a backwards integrated basin of escape (top panel) at $e_J = -203.75205349030903$. We use the same initial conditions for the backwards integrated orbits as for the forward integrated ones. The red (and yellow) regions correspond to initial conditions for which the escaping star passes L_1 (or L_2). The black regions correspond to initial conditions for which the orbit does not escape. For the backwards integration, the following modifications must be made in the numerical integration of the orbits:

- (i) The sign of the time step in the Runge-Kutta integrator must be reversed,
- (ii) the sign of the velocities in the equations of motion (6) must be reversed,
- (iii) the sign of the frequencies in the equations of motion (6) must be reversed,
- (iv) the sign of the velocities in the definition of the surface of section must be reversed.

The chaotic or strange saddle (an invariant chaotic set) is given by the intersection of its stable and unstable manifolds. The stable (unstable) manifolds of the chaotic set coincide with the boundaries between the forwards (backwards) integrated L_1 - and L_2 -basins of escape (c.f. Aguirre et al. 2001). The stable and unstable manifolds as well as the corresponding basins of escape are symmetric to each

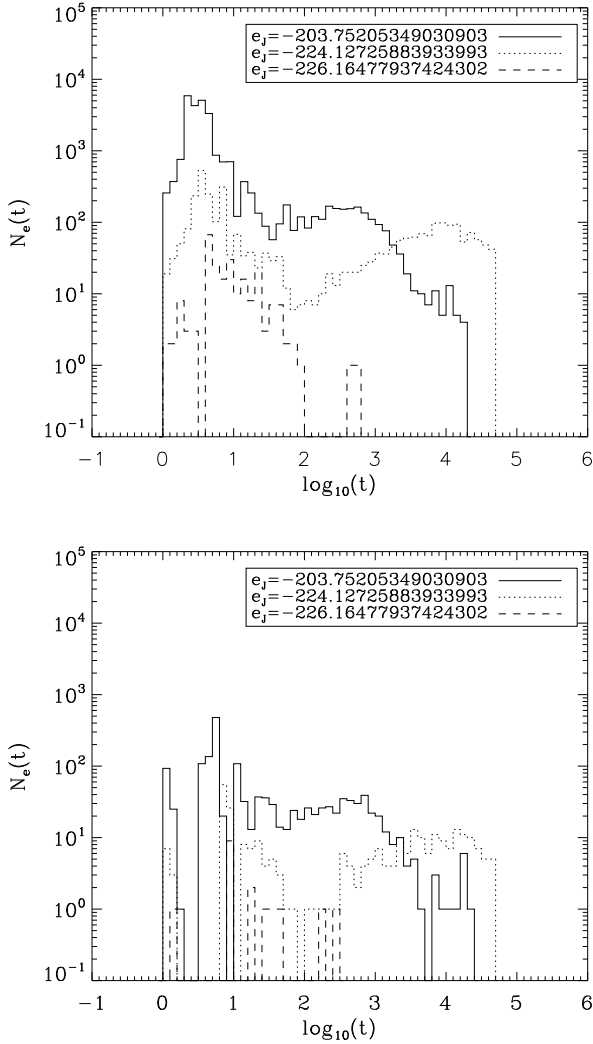


Figure 8. Differential distributions of escape times. Top panel: For the $x - y$ basins of escape of Figure 5. Bottom panel: For the $x - v_x$ basins of escape of Figure 5. Solid lines: $e_J = -203.75205349030903$, dotted lines: $e_J = -224.12725883933993$, dashed lines: $e_J = -226.16477937424302$.

other due to the time symmetry of the equations of motion (6). In a non-hyperbolic system, there may be tangencies between the stable and unstable manifolds, i.e. the splitting angle between them may be zero. A comparison of Figure 5 and Figure 6 reveals that, in contrast to the system studied in Ernst et al. (2008), the phase-spatial extent of the chaotic saddle for the present system is tiny as compared to the squared Lagrangian radius. For this reason we did not calculate the chaotic saddle for the system studied in the present work.

Figure 7 shows the distribution of escape times t_e on surfaces of section for the forwards integration at $e_J = -203.75205349030903$ (left panel) and $e_J = -224.12725883933993$ (right panel). The scale on the color bar is logarithmic. The region within the separatrix, from which orbits do not escape, is overplotted with black dots and invariant curves on the grey-shaded area. In particular,

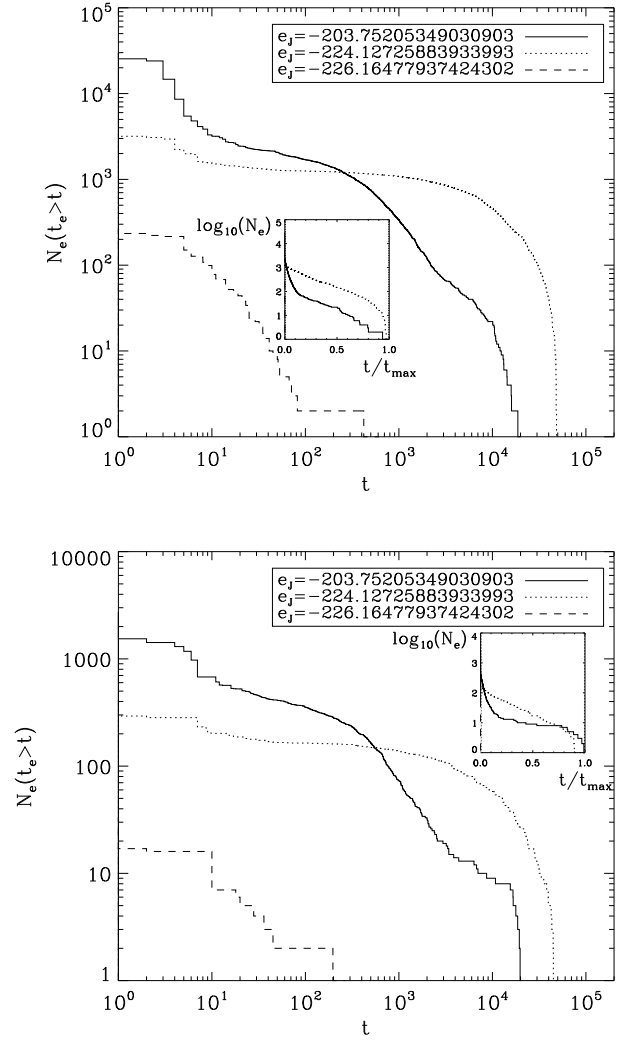


Figure 9. Complementary cumulative distributions of escape times. Top panel: For the $x - y$ basins of escape of Figure 5. Bottom panel: For the $x - v_x$ basins of escape of Figure 5. Solid lines: $e_J = -203.75205349030903$, dotted lines: $e_J = -224.12725883933993$, dashed lines: $e_J = -226.16477937424302$. The sharp drop-offs of the solid curves at $t \approx 20000 = t_{\max}$ and of the dashed curves at $t \approx 50000 = t_{\max}$ are due to the artificial cutoffs in the calculation program and the fact that only the escaping orbits have been included in the statistics. The linear-logarithmic insets show the evolution for the two lowest Jacobi energies. The histogram for the highest Jacobi energy is not shown in the inset due to the low number of escaping orbits. The curves in the insets indicate a transition to an exponential decay in the limit of long escape times, except for the solid curve in the lower panel's inset.

Figure 7 shows that there are chaotic orbits which do not escape within time t_{\max} .

Figure 8 shows the differential distributions of escape times, i.e. the escaper number N_e as a function of time t . The top panel shows the distributions for the $x - y$ basins of escape of Figure 5. The bottom panel shows the distributions for the $x - v_x$ basins of escape of Figure 5. The solid lines correspond to $e_J = -203.75205349030903$, the dotted lines correspond to $e_J = -224.12725883933993$, and

the dashed lines correspond to $e_J = -226.16477937424302$. The distributions are irregularly shaped, i.e. they are not monotonically.

In contrast, Figure 9 shows the complementary cumulative distributions of escape times on surfaces of section. The x axis shows the time t , the y axis shows the escaper number with escape time $t_e > t$, which is proportional to the exceedance or survival probability (c.f. Altmann et al. 2013). As for Figure 8, the top panel shows the decay for the $x - y$ basins of escape of Figure 5. The bottom panel shows the decay for the $x - v_x$ basins of escape of Figure 5. The solid lines correspond to $e_J = -203.75205349030903$, the dotted lines correspond to $e_J = -224.12725883933993$, and the dashed lines correspond to $e_J = -226.16477937424302$. The sharp drop-off of the solid curves at $t \approx t_{\max} = 20000$ and of the dashed curves at $t \approx t_{\max} = 50000$ is due to the artificial cutoffs in the calculation program and the fact that only the escaping orbits have been included in the statistics. For a galaxy which has the size of, say, NGC 1300, the system of units (2) - (4) yields that these maximum times correspond to 2000 and 5000 Gyr, respectively, both of which are well above 100 Hubble times. The linear-logarithmic insets show the evolution for the two lowest Jacobi energies. The histogram for the highest Jacobi energy is not shown in the inset due to the low number of escaping orbits. The curves in the insets, except for the solid curve in the lower panel's inset, indicate a transition to an exponential decay law in the limit of long escape times. The slope of the exponential decay law characterizes the strange chaotic saddle (Kadanoff & Tang 1984). It can be seen that the solid curve in the lower panel's inset is, in contrast to the other curves in the insets, not straight in the shown range. The reason may be that for this parameter set the chaotic saddle vanishes.

3.4 Spiral arms

In the case of star clusters, escaping orbits form so-called tidal tails (Odenkirchen et al. 2003; Di Matteo et al. 2005; Küpper et al. 2008; Just et al. 2009; Ernst 2009; Küpper et al. 2010; Berentzen & Athanassoula 2012). Based on the similarity of the corresponding effective potentials, we would like to point out here the striking similarity between spiral arms of barred spiral galaxies and star cluster tidal tails and mention the hypothesis that the spiral arms of barred spiral galaxies such as NGC 1300 are the equivalent of such star cluster tidal tails forming in an effective potential similar to that of Eqn. (1) below which has two saddle points (see Figure 1 for the case of a two-armed barred spiral galaxy). Since star cluster tidal tails follow the curvature of the orbit of the star cluster around the galactic centre, they are nearly straight for orbits with large galactocentric distances (see Figure 1 in Just et al. 2009, with the effective potential shown in their Figure 2). On the other hand, the spiral arm “tidal tails” of barred spiral galaxies are not caused by the tidal field but by the non-axisymmetric bar-like perturbation, wind up around the banana-shaped isolines of the effective potential in which L_4/L_5 are enclosed and form the spiral-like shape which is prominent in barred spirals with two spiral arms which emerge from the ends of the bar (Binney & Tremaine 2008, Plate 10 showing NGC 1300).

In Figure 10 we show at $e_J = -224.12725883933993$ that this scenario is viable. We have modified our integration

program for the calculation of the basins of escape to yield output of all orbit trajectories for a three-dimensional grid of size $N_x \times N_y \times N_{v_x} \approx 11 \times 800 \times 3$ with $\Delta x = 4.0$, $\Delta y = 0.025$ and $\Delta v_x = 5.0$. The grid is centred in the origin of phase space coordinates. We allow for both signs of v_y . The snapshot in the left-hand panel of Figure 10 shows that at $t = 7.5$, which corresponds to 750 Myrs in the units given by Eqns. (2) - (4), two spiral arms with a similar morphology to those in Patsis (2006, his Figure 1) have formed. The snapshot in the right-hand panel of Figure 10 shows the situation at $t = 10.0$ (1 Gyr), where a ring has formed. The standard orbit integration routine, which is used to obtain Figure 4, plots a point at every integration step. However, in Figure 10, the density of points along one stellar orbit is taken to be proportional to the velocity of a particle. In particular, a point is plotted, if an integer counter variable, which is increased by one in every integration step, exceeds the velocity of the particle. In such a way we simulate a real N -body simulation of such a system: The density of particles will be highest where the velocity is lowest. Similarly, clumps form in tidal tails of star clusters at positions where the velocity of the escaping particles is lowest (Küpper et al. 2008).

The two morphologies in Figure 10 are also discussed in the papers by Athanassoula et al. (2009a,b). These papers provide the connection between the bar strength and the corresponding morphological types. For example, they predict that, if the non-axisymmetric forcing is relatively low the resulting morphology will be an R_1 or R'_1 ring while if it is stronger, it will be a spiral or one of the remaining types of rings (R_2, R_1R_2 etc.). In our case, we see that the evolutionary state of the barred spiral galaxy is of relevance as well. Rings may be more evolved than spirals (cf. Athanassoula 2012).

4 DISCUSSION

We have studied the region in the close vicinity of and inside the critical volume of a galactic potential with a bar. The critical volume is defined as the volume which encloses the last closed equipotential surface of the effective potential. The present paper is complementary to the series of papers by Athanassoula et al. (2009a,b, 2010); Athanassoula (2012). While the latter papers are concerned with the morphology, application of the manifold theory to and comparison with real galaxies, the present paper gives quantitative information on the escapes. We have particularly studied the physics in the barred four-component effective potential in Eqn. (1) by Zotos (2012b). We have calculated Poincaré surfaces of section and the basins of escape at different values of the Jacobi energy, a few examples of typical orbits, the distribution of escape times on a surface of section, differential and complementary cumulative distributions of escape times. We have also studied the behaviour of the escaped particles outside of the Lagrangian radius, where they form spiral arms or a ring.

We state the main conclusions of this work, which are valid for the system given by Eqn. (1) with our corresponding choice of the parameters, as follows:

- (i) We have found numerical evidence for the existence of

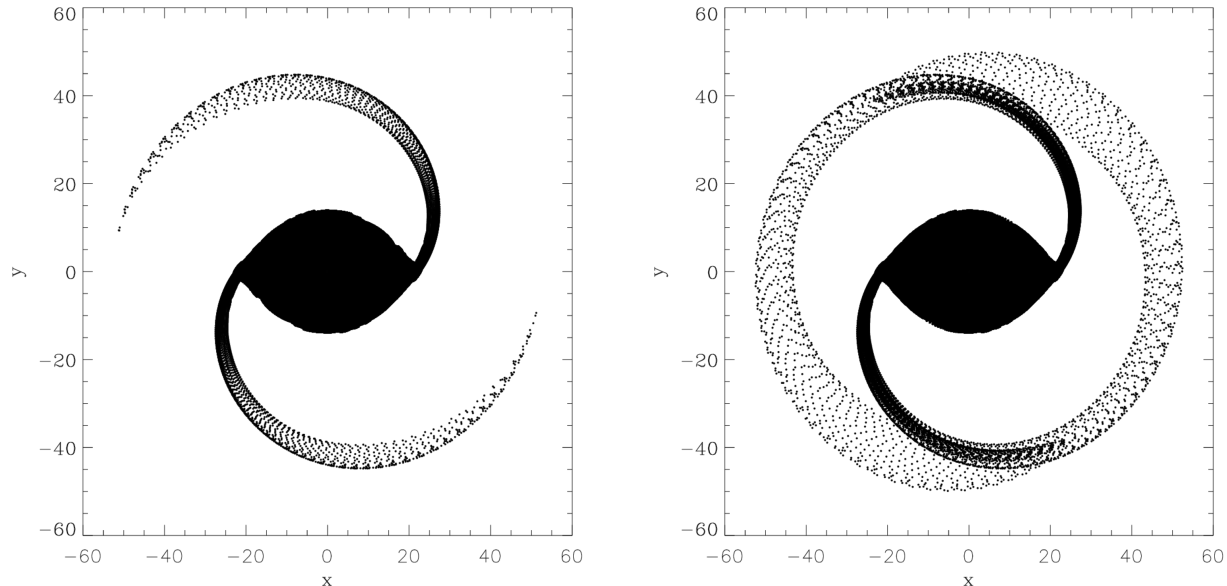


Figure 10. Formation of spiral arms and a ring at $e_J = -224.12725883933993$ in the effective potential of Eqn. (1). Left: At $t = 7.5$. Spiral arms have formed. Right: At $t = 10.0$. A ring has formed.

a separatrix in phase space in both the Poincaré surfaces of section and the basins of escape which hinders particles from escaping out of the bar region. While the adelic integral hinders quasiperiodic orbits from escaping, the separatrix prevents chaotic orbits from escaping. We have found that there are chaotic orbits which do not escape within t_{\max} .

(ii) (a) The late-time exponential decay related to the chaotic saddle is not relevant for a NGC 1300 sized barred galaxy since the corresponding escape times are well above a Hubble time. However, the early-time escape process within a Hubble time is relevant (see Figure 8). Note that these two statements still hold for a galaxy which has one tenth the size in both x and y directions and one hundredth of the mass of NGC 1300.

(b) The phase-spatial extent of the chaotic saddle is tiny as compared with the squared Lagrangian radius.

(iii) We have presented evidence for a striking similarity of spiral arms of barred spiral galaxies to tidal tails of star clusters.

Future research may put the above-mentioned conclusion (i), (ii) (a) and (b), which hold for the special case of the potential of Eqn. (1), on firmer grounds with more numerical evidence for other cases with modified bar potentials as those used in Athanassoula et al. (2009a,b, 2010) and identify them as generally valid in typical barred galactic potentials or falsify them for the general case of galactic potentials with bars.

Concerning conclusion (iii), if it is true that the spiral arms of barred spiral galaxies are formed out of escaping particles from the bar region we may think of the formation scenario of barred spiral galaxies as follows (cf. Athanassoula 2012):

- (i) An axisymmetric rotating stellar system forms.
- (ii) At a certain redshift the system gets unstable to the

formation of a bar (i.e. it develops a non-axisymmetric bar-like perturbation).

(iii) Escaping particles with Jacobi energies higher than the critical one form spiral arms (similar to the formation of tidal tails in star clusters). At the same time the bar strength decreases as witnessed in Athanassoula (2012).

(iv) The barred spiral galaxy has formed.

Future N -body simulations may elaborate the different shapes and morphologies of barred spiral galaxies (e.g. Buta 2011) and measure the amplitudes of the spiral perturbations. Moreover, results from the theory of the dissolution of star clusters may be applied to the problem of the formation of barred spiral galaxies. Also, the manifold flux-tube theory of Athanassoula et al. may be applied to the formation of tidal tails in star clusters.

5 ACKNOWLEDGEMENTS

Both authors would like to thank Dr. Thorsten Lisker for pointing out a few references to them and the anonymous referee for thoughtful comments on the manuscript which greatly helped to improve the paper. AE acknowledges partial financial support by grant JU 404/3-1 of the Deutsche Forschungsgemeinschaft (DFG) and hospitality and partial financial support through Silk Road Project at National Astronomical Observatories of Chinese Academy of Sciences (NAOC) in Beijing, China, Grant Number 2009S1-5. TP acknowledges financial support through a Forschungskredit of the University of Zürich, grant no. FK-13-112. The APOD website (<http://apod.nasa.gov>) has been used as a further source of information.

REFERENCES

- Aguirre J., Vallejo C., Sanjuán M. A. F., 2001, *Phys. Rev. E*, 64, 066208
- Aguirre J., Viana R. L., Sanjuán M. A. F., 2009, *Rev. Mod. Phys.*, 81, 333
- Aguirregabiria J. M., 1997, *Phys. Lett. A*, 224, 234
- Altmann E. G., Portela J. S. E., Tél T., 2013, *Rev. Mod. Phys.*, 85, 869
- Athanassoula E., 2012, *MNRAS*, 426, L46
- Athanassoula E., Bienayme O., Martinet L., Pfenniger D., 1983, *A&A*, 127, 349
- Athanassoula E., et al., 2009a, *MNRAS*, 394, 67
- Athanassoula E., et al., 2009b, *MNRAS*, 400, 1706
- Athanassoula E., Romero-Gómez M., Bosma A., Masdemont J. J., 2010, *MNRAS*, 407, 1433
- Athanassoula E., Romero-Gómez M., Masdemont J. J., 2011, *Memorie della Societa Astronomica Italiana Supplementi*, 18, 97
- Benet L., Seligman T. H., Trautmann D., 1999, *Cel. Mech Dyn. Astron.*, 71, 167
- Benet L., Trautmann D., Seligman T. H., 1996, *Cel. Mech Dyn. Astron.*, 66, 203
- Berentzen I., Athanassoula E., 2012, *MNRAS*, 419, 3244
- Binney J., Tremaine S., 2008, *Galactic Dynamics*, second edn. Princeton University Press
- Bleher A., Grebogi C., Ott E., R. B., 1988, *Phys. Rev. A*, 38, 930
- Bleher S., Grebogi C., Ott E., 1990, *Phys. D*, 46, 87
- Bleher S., Ott E., Grebogi C., 1989, *Physical Review Letters*, 63, 919
- Boyd P. T., McMillan S. L. W., 1992, *Phys. Rev. A*, 46, 6277
- Boyd P. T., McMillan S. L. W., 1993, *Chaos*, 3, 507
- Buta R. J., 2011, *ArXiv e-prints*
- Caranicolas N. D., Karanis G. I., 1998, *Ap&SS*, 259, 45
- Chen Q., Ding M., Ott E., 1990, *Phys. Lett. A*, 145, 93
- Contopoulos G., 1983a, *ApJ*, 275, 511
- Contopoulos G., 1983b, *A&A*, 117, 89
- Contopoulos G., 1990, *A&A*, 231, 41
- Contopoulos G., Harsoula M., Lukes-Gerakopoulos G., 2012, *Cel. Mech Dyn. Astron.*, 113, 255
- Contopoulos G., Kandrup H. E., Kaufmann D., 1993, *Phys. D*, 64, 310
- Contopoulos G., Kaufmann D., 1992, *A&A*, 253, 379
- Contopoulos G., Papayannopoulos T., 1980, *A&A*, 92, 33
- Contopoulos G., Varvoglis H., Barbanis B., 1987, *A&A*, 172, 55
- de Moura A. P. S., Letelier P. S., 2000, *Phys. Rev. E*, 62, 4784
- de Vaucouleurs G., 1963, *ApJSS*, 8, 31
- Di Matteo P., Capuzzo Dolcetta R., Mocchi P., 2005, *Celestial Mechanics and Dynamical Astronomy*, 91, 59
- Ding M., Grebogi C., Ott E., Yorke J. A., 1990, *Phys. Rev. A*, 42, 7025
- Eckhardt B., 1987, *J. Phys. A*, 20, 5971
- Eckhardt B., 1988, *Phys. D*, 33, 89
- Eckhardt B., Jung C., 1986, *J. Phys. A*, 19, L829
- Ernst A., 2009, PhD thesis, University of Heidelberg, Germany, <http://www.ub.uni-heidelberg.de/archiv/9375>
- Ernst A., Just A., Spurzem R., Porth O., 2008, *MNRAS*, 383, 897
- Fukushige T., Heggie D. C., 2000, *MNRAS*, 318, 753
- Gaspard P., Rice S. A., 1989, *J. Chem. Phys.*, 90, 2225
- Hasan H., Norman C., 1990, *ApJ*, 361, 69
- Hasan H., Pfenniger D., Norman C., 1993, *ApJ*, 409, 91
- Hénon M., 1988, *Phys. D*, 33, 132
- Hénon M., Heiles C., 1964, *AJ*, 69, 73
- Hohl F., 1971, *ApJ*, 168, 343
- Hut P., 1983, *AJ*, 88, 1549
- Hut P., Bahcall J. N., 1983, *ApJ*, 268, 319
- José J. V., Rojas C., Saletan E. J., 1992, *Amer. J. Phys.*, 60, 587
- Jung C., 1987, *J. Phys. A*, 20, 1719
- Jung C., Lipp C., Seligman T. H., 1999, *Ann. Phys.*, 275, 151
- Jung C., Mejia-Monasterio C., Seligman T. H., 1995, *Phys. Lett. A*, 198, 306
- Jung C., Pott S., 1989, *J. Phys. A*, 22, 2925
- Jung C., Richter P. H., 1990, *J. Phys. A*, 23, 2847
- Jung C., Scholz H. J., 1987, *J. Phys. A*, 20, 3607
- Jung C., Tél T., 1991, *J. Phys. A*, 24, 2793
- Just A., Berczik P., Petrov M. I., Ernst A., 2009, *MNRAS*, 392, 969
- Kadanoff L. P., Tang C., 1984, *Proc. Natl. Acad. Sci.*, 81, 1276
- Küpper A. H. W., Kroupa P., Baumgardt H., Heggie D. C., 2010, *MNRAS*, 401, 105
- Küpper A. H. W., MacLeod A., Heggie D. C., 2008, *MNRAS*, 387, 1248
- Lai Y.-C., de Moura A. P. S., Grebogi C., 2000, *Phys. Rev. E*, 62, 6421
- Lai Y.-C., Grebogi C., Blümel R., Kan I., 1993, *Physical Review Letters*, 71, 2212
- Lau Y.-T., Finn J. M., Ott E., 1991, *Physical Review Letters*, 66, 978
- Lipp C., Jung C., 1999, *Chaos*, 9, 706
- Lyapunov A., 1949, *Ann. Math. Studies*, 17
- Martinet L., Udry S., 1990, *A&A*, 235, 69
- Masters K. L., Nichol R. C., Hoyle B., Lintott C., Bamford S. P., Edmondson E. M., Fortson L., Keel W. C., Schawinski K., Smith A. M., Thomas D., 2011, *MNRAS*, 411, 2026
- Melvin T., Masters K., the Galaxy Zoo Team 2013, *Memorie della Societa Astronomica Italiana Supplementi*, 25, 82
- Miller R. H., Prendergast K. H., Quirk W. J., 1970, *ApJ*, 161, 903
- Motter A. E., Lai Y.-C., 2002, *Phys. Rev. E*, 65, 015205
- Navarro J. F., Henrard J., 2001, *A&A*, 369, 1112
- Odenkirchen M., Grebel E. K., Dehnen W., Rix H.-W., Yanny B., Newberg H. J., Rockosi C. M., Martínez-Delgado D., Brinkmann J., Pier J. R., 2003, *AJ*, 126, 2385
- Ostriker J. P., Peebles P. J. E., 1973, *ApJ*, 186, 467
- Ott E., 2002, *Chaos in dynamical systems*, second edn. Cambridge University Press
- Patsis P. A., 2006, *MNRAS*, 369, L56
- Pfenniger D., 1984, *A&A*, 134, 373
- Romero-Gómez M., Athanassoula E., Masdemont J. J., García-Gómez C., 2007, *A&A*, 472, 63
- Romero-Gómez M., Masdemont J. J., Athanassoula E., García-Gómez C., 2006, *A&A*, 453, 39
- Rückerl B., Jung C., 1994, *J. Phys. A*, 27, 55

- Schneider J., Tél T., Neufeld Z., 2002, *Phys. Rev. E*, 66, 066218
- Sellwood J. A., 1980, *A&A*, 89, 296
- Seoane J. M., Aguirre J., Sanjuán M. A. F., Lai Y.-C., 2006, *Chaos*, 16, 023101
- Seoane J. M., Sanjuán M. A. F., 2008, *Phys. Lett. A*, 372, 110
- Seoane J. M., Sanjuán M. A. F., 2013, *Rep. Prog. Phys.*, 76, 016001
- Seoane J. M., Sanjuán M. A. F., Lai Y.-C., 2007, *Phys. Rev. E*, 76, 016208
- Sheth K., Elmegreen D. M., Elmegreen B. G., Capak P., Abraham R. G., Athanassoula E., Ellis R. S., Mobasher B., Salvato M., Schinnerer E., Scoville N. Z., Spalsbury L., Strubbe L., Carollo M., Rich M., West A. A., 2008, *ApJ*, 675, 1141
- Simó C., 2014, *Dynamical properties in Hamiltonian Systems. Applications to Celestial Mechanics. Text of the lectures delivered at the Centre de Recerca Matemàtica on January 27-31, 2014.*
- Siopis C., Kandrup H. E., Contopoulos G., Dvorak R., 1996, *Cel. Mech Dyn. Astron.*, 65, 57
- Sweet D., Ott E., 2000, *Phys. Lett. A*, 266, 134
- Teuben P. J., Sanders R. H., 1985, *MNRAS*, 212, 257
- Zotos E. E., 2011, *New Astron.*, 16, 391
- Zotos E. E., 2012a, *New Astron.*, 17, 576
- Zotos E. E., 2012b, *Research in Astr. Astrophys.*, 12, 500
- Zotos E. E., 2012c, *ApJ*, 750, 56

This paper has been typeset from a $\text{T}_{\text{E}}\text{X}$ / $\text{L}^{\text{A}}\text{T}_{\text{E}}\text{X}$ file prepared by the author.